https://doi.org/10.1016/j.matdes.2016.10.076

# Exploiting the non-equilibrium phase transformation in a 15Cr-2Ni-2Al-11Mn resource-saving Duplex stainless steel

Jianquan Wan, Haihui Ruan*, Jianbiao Wang, Sanqiang Shi

Department of Mechanical Engineering, The Hong Kong Polytechnic University, Hung Hom, Kowloon, Hong Kong, China

## Abstract

Though most duplex stainless steels are quenched from high temperature, at which the equilibrium phase constitution is close to the desired magnitude, this work explored the non-equilibrium phase transformation in duplex stainless steel and showed that duplex stainless steels of equilibrated primary phase content can be obtained through different thermomechanical processes and exhibit disparate microstructures and mechanical property. Specifically, we studied the effects of annealing temperature, time, cooling method and plastic deformation based on the 15Cr-2Ni-2Al-11Mn DSS and established TTT diagrams of as-cast and cold-rolled duplex stainless steels using the Avrami equation, respectively. A simplified model of diffusion-mediated phase transformation was established to explain the stretched exponent 2.5 used in the Avrami equation. And it is found that plastic deformation not only changes the rate of phase transformation and the grain size of new phase but also changes the equilibrium phase constitution.

**Key words:** Duplex stainless steel; Microstructure; Phase transformation; Plastic deformation; TTT diagram

---

* Corresponding author: Tel./fax: + 852 2766 6648.
E-mail address: haihui.ruan@polyu.edu.hk (Haihui Ruan).

# 1. Introduction

Owing to the ever-increasing needs of materials with both high mechanical strength and high corrosion resistance, duplex stainless steel (DSS) becomes more preferred over the conversional single-phase stainless steel. Nowadays the commercially available DSSs exhibit at least twice the yield strength, and similar or higher corrosion resistance of their austenitic counterparts, which have partially replaced austenitic stainless steels (ASS) such as 316 or 304 stainless steels in stringent service environment [1-5]. The replacement is not only propelled by the better combination of mechanical strength and corrosion resistance but also owing to the possibility to reduce the strategic element nickel and chromium [6] in stainless steels. This work is based on the recently developed 15Cr-2Ni DSS [7], in which aluminium and manganese were alloyed such that the ferrite former and austenite former, in terms of Cr-equivalent ($Cr_{eq}$) and Ni-equivalent ($Ni_{eq}$) composition, can lead to a balanced content of both primary phases based on the Schaeffler-type diagram [8]. Since the 15Cr-2Ni series DSSs exhibit compelling properties as introduced in [7], more detailed investigation is worthy.

Our focus is on the influence of heat treatment parameters, such as annealing temperature, time, cooling rate as well as plastic deformation and to establish time-temperature-transformation (TTT) diagram of the transformation of primary phases. This is motivated by the consideration that the non-equilibrium phase transformation, which is ubiquitous in producing DSS, should be more thoroughly explored such that the microstructure can be better controlled (say, to reduce grain size). In the open literature, many investigations have exhibited the important effects of process parameters of post-cast thermomechanical treatment. For example, Sohn *et al.* [9] investigated the effect of annealing temperature on microstructural and mechanical properties of Fe-0.35C-3.5Mn-5.8Al alloy. Li *et al.* [10] investigated the effect of annealing time on the content, distribution and shape of ferrite phase in DSS. Chen *et al.* [11] demonstrated that cooling rate is critical for the adjustment of the volume fraction of primary phases. They analysed the phase content in the welding-induced heat affected zone of DSS 2304 and found that austenite content increased gradually from 27.8 % to 35.7% as the cooling rate decreased from 100 to 10 °C/s. Plastic deformation increases the amount of sigma phase precipitation in 2205 DSS [12], and the deformation brings about ferromagnetic martensite in the DSS UNS S31830 [13]. Kim *et al.* [14, 15] constructed TTT diagram for sigma phase in CD3MN and CD3MWCuN DSS. Although the non-equilibrium evolution of primary phase in DSS has been studied in welding process [16, 17], the TTT diagram of primary phase transformation in DSS is rarely found in the open literature. This can probably be ascribed to the fact that the solution treatment for adjusting phase content in DSS is quite unified. Most of the solution treatment of DSS is based on the notion of quenching equilibrium phase content of a high temperature. Therefore, TTT diagram of non-equilibrium phase transformation is seemingly not crucial. In this work, through establishing the TTT diagrams of primary phase transformation in DSS, we would like to show that DSS of equilibrated phase content may be achieved under different solution treatment temperature since the non-equilibrium phase transformation can be utilized.

## 2. Experimental

The present study is based on 15Cr-2Ni-2Al-11Mn alloy which leads to about 20% ferrite phase based on the Schaeffler diagram. The raw materials were melted in an electric arc furnace and then fast solidified into a copper mould at room temperature, which resulted in about 70% ferrite phase in the as-cast alloy. The iron-manganese alloy was used in melting in order to minimize the evaporation of manganese in the arc furnace. The resulted chemical composition of the as-cast alloy is checked through spectroscopic analysis and shown in Table 1. The as-cast (AC) samples were wire-cut into several straps and some of them were cold-rolled (CR) with 70% thickness reduction. The AC and CR samples were then isothermally hold at 750~1250 °C for 1~240 min and finally quenched in water quenching (W) or cooled in ambient air (A) or in furnace (F) to room temperature, respectively. All samples were electrolytically etched in 15 wt.% KOH solution, which makes the austenite bright and the ferrite grey under an optical microscope. The optical images from ten randomly selected areas (approximately 0.73 $mm^2$) of the etched surface were taken using a 200x objective lens in order to analyze the morphology and fraction of ferrite phase using the metallography image analysis software. The volume fraction of a primary phase is considered to be the average area fraction of the ten images based on the assumption that the area fraction is identical at different depths. To validate this assumption, we ground some samples and found the difference of area fraction at different depth is within 2% of the average value. On the other hand, all samples were cut from the same depth of the ingot in order to minimize the effect of inhomogeneity. Selected samples were subjected to investigation using transmission electron microscope (TEM, JEOL 2000FX working at 200 kV). The sample was thinned into 30 μm by sand paper, punched into wafers of 3 mm diameter and ion milled to get the TEM foils.

# 3. Results

## 3.1 An overview of microstructures after different heat treatments

In order to let reader has a quick overview of the effect of annealing temperature, time, cooling rate and plastic deformation, we select five samples for a brief description. Fig. 1(a) shows the result using the conventional approach, in which the CR sample isothermally hold at 1050 °C for 30 minutes and finally water quenched, therefore denoted as CR-1050-30-W. The $\gamma$ phase, amounting to 41% volume, is those white islands embedded in the continuous $\delta$ phase matrix. No secondary precipitates were found in the ferrite-ferrite and ferrite-austenite phase boundaries. The two phases were further confirmed by XRD analysis as shown in Fig. 1(b). In Fig. 1(b), the effect of cooling rate is also exhibited in terms of the change of the relative height of the peaks pertaining to the $\gamma(111)$ and $\delta(110)$ planes. After the analysis of optical micrographs of CR samples heated at 1050 °C for 30 mins, it is revealed that the volume fraction of $\gamma$ phase $\phi_\gamma$ increases from 41% to 62%, when the cooling rate reduces from water quenching to furnace cooling.

The annealing at lower temperature leads to much smaller but the larger quantity of separated γ phase. This is demonstrated by the sample CR-850-30-W shown in Fig. 1(c). Longer annealing time makes the γ phase larger and coalesced, which is exemplified in Fig. 1(d) for the case of CR-850-90-W. And slow cooling also provides more time for the growth and coalesces of γ phase. In the sample CR-850-30-F shown in Fig. 1(e), γ phase is larger and more equiaxed than that in CR-850-30-W. In order to demonstrate the effect of plastic deformation, Fig. 1(f) shows the sample AC-850-30-W. The comparison with CR-850-30-W (Fig. 1(c)) indicates that plastic deformation leads to much smaller γ phase. The dual-phase microstructure can be further confirmed using TEM. Fig. 2 shows the interface of δ and γ grains taken from CR sample solution-treated at 750 °C for 30 min followed by water quenching.

### 3.2 The quantitative effects of annealing temperature, time and cooling rate

The variations of the volume fraction of the ferrite phase $\phi_\delta$ against annealing temperature $T$ for different annealing time is summarized in Fig. 3. It should be noted that the ferrite content is the water-quenched result instead of the high-temperature result. Fig. 3 illustrates two cases. For Case I, the annealing time is set to 30 minutes. For case II, the annealing time is sufficient long that the quenched ferrite content does not change further with longer time. We name it quasi-equilibrium content since they are not the exact high-temperature value but the quenched result.

The two cases shown in Fig. 3 are remarkably different especially in the temperature range of 750 ~ 1050 °C. This manifests the influence of annealing time and indicates that annealing for 30 min at 750 ~ 1050 °C is insufficient for equilibrating phases. For the case I, the content of ferrite phase decreases with annealing temperature $T$ when it is lower than 1050 °C, which is seemingly against the general understanding that more ferrite phase will be transformed to austenite phase at lower temperature. Based on case II, it is clear that the equilibrium ferrite content increase with temperature. It is noted that when $T$ is higher than 1050 °C, the ferrite content surges. The microstructure became almost fully ferritic at 1150 °C for the CR samples and 1250 °C for the AC ones. Since the as-cast material contains about 70% ferrite, the critical temperature $T_{cr}$ can be concluded, below which the net phase transformation is ferrite-to-austenite and vice-versa. $T_{cr}$ shall be a temperature between 1050 and 1150 °C.

The different tendency of phase transformation when $T$ is lower or higher than $T_{cr}$ can further be elucidated using the short-duration of 1 min and 10 s isothermal treatment (followed by water quenching). Fig. 4(a) and Fig. 4(b) show the micrographs of CR-950-1-W and CR-1150-0.17-W, respectively. In Fig. 4(a), it is observed that $\gamma_2$ phase of scale-like morphology nucleates in grain boundary and ferrite phase interior. In Fig. 4(b), the austenite islands are decomposed from the boundary. This decomposition process leaves the feather-like austenite phase, which may be the consequence of heterogeneous diffusion [18, 19]. Heterogeneous diffusion herein refers to the fact that interphase diffusion is faster when the surface-area-to-volume ratio is larger. In DSS, the γ-to-δ transition involves the change of concentration of elements. Austenite-stabilizing elements such as Ni and Mn must diffuse out of the newly formed δ phase into the remaining $\gamma$ phase. Therefore, if there is a small protrusion in γ-δ phase boundary, the newly formed δ phase over there has larger surface area than other places, expediting outward diffusion. This protrusion then grows further and faster into the γ phase, leading to the feather-like microstructure as shown in Fig. 4(b).

The effect of cooling rate for Case I is summarized in the inset of Fig. 3, in which the water quenched samples were used as reference. That is, the results indicate the difference of ferrite content $\Delta\phi_\delta$ if the cooling rate reduces from that of the water quenching. The air and furnace cooling only lead to no more than 5% and 21% reduction in ferrite content respectively when the temperature is below 1050 °C. The magnitude of reduction rises more or less linearly with temperature. This difference $\Delta\phi_\delta$ quickly increases with temperature when the temperature is higher. However, it should be noted that the difference significantly reduces when the sample is cooled from 1250 °C, at which the material becomes fully ferritic. Even furnace cooling cannot notably increase the content of austenite. After investigating the microstructures of the sample heated at 1250 °C, it is found that the ferritic grains have grown to be very large, which minimizes grain boundaries and makes the nucleation site of $\gamma$ phase very rare.

### 3.3 TTT diagrams based on water quenched samples

Ferrite-to-austenite transformation occurs at 750~1050 °C, so the TTT diagram for both AC and CR samples heat treated below 1050 °C followed by water quenching were established. The results are fitted using the Avrami equation [20, 21]:

$$f = \phi_\gamma / \phi_\gamma^e = 1 - \exp(-(t/\tau)^n) \tag{1}$$

Where $f$ is the fraction transformed, $\phi_\gamma$ is the volume fraction of austenite phase at time $t$, $\phi_\gamma^e$ is the volume fraction of austenite phase at the thermal equilibrium state, which is determined based on the experimental results when the $\phi_\gamma$ remains unchanged if the annealing time is doubled. Since the samples have 30% austenite phase before heat treatment, we assume the time in Eq. (1) does not start from zero but from $t_0$. Therefore, Eq. (1) is modified to:

$$\phi_\gamma / \phi_\gamma^e = 1 - \exp(-((t + t_0)/\tau)^n)\,. \tag{2}$$

Eq. (2) can be recast as:

$$\ln(-\ln(1 - \phi_\gamma / \phi_\gamma^e)) = n \ln(t + t_0) - n \ln \tau\,, \tag{3}$$

The exponent $n$ is considered to be close to 2.5, which is based on a simplified model for diffusion mediated phase transformation, to be described in section 4.1. Therefore, in fitting the data points, the initial time $t_0$ is adjusted to ensure that the experimental data points are along the straight line. Fig. 5 shows the experimental data and fitting lines in the log-log plot. The magnitudes of fitting parameters $n$, $\tau$, $t_0$, $\phi_\gamma^e$ are listed in Table 2.

The Avrami equations were then used to establish TTT diagrams of austenite formation, as shown in Fig. 6. It is noted that the growth rate of austenite phase increases with annealing temperature and that the austenite formation in AC samples is faster than that in CR samples. If we define the time needed for austenite content increasing from 0% to 1% as the breeding time, the breeding time is about 80-90 min at 750 °C and 1-2 min at 1050 °C for both AC and CR samples.

As an exemplified usage of the TTT diagram and the effect of cooling rate, a series of DSS samples of all about 50% ferrite phase content were obtained. These samples were marked as CR-1000-15-A, CR-1000-30-A, AC-1000-30-A, AC-750-180-W, CR-750-90-A, which indicate the respective heat-treatment process. The mechanic properties are listed in Table 3, and the corresponding metallographs are shown in Fig. 7. The results indicate that a large variation of mechanical properties as well as microstructures can be obtained by changing the heat-treatment parameters. In particular, reducing annealing temperature or time can retard the growth of austenite and ferrite grains, which is the cause of the relatively higher strength of the samples CR-1000-15-A and CR-750-90-A.

# 4. Discussion

## 4.1 An explanation of $n = 2.5$ based on diffusion-mediated phase transformation

The theoretical investigations of the variation of primary phases were only conducted for DSSs with a substantial amount of nitrogen [17, 22, 23], and the diffusion of nitrogen was considered to be the main reason for the evolution of phase constitution. However, this is not the case for the DSS investigated in this work. In order to understand the phase evolution in our material, the following assumptions are made: (i) the transformation between austenite and ferrite is governed by the diffusion of substances; (ii) the diffusion is due to the exchange of position between vacancy and solute atom and (iii) the interphase boundaries serve as vacancy reservoirs to assist the flow of substances. Firstly the conservation law of a substance *i* is given as:

$$\frac{d}{dt}\left(\int_{V_\delta} C_i dV + \int_{V_\gamma} C_i dV\right) = 0, \tag{4}$$

where $C$ denotes the local concentration, $V_\delta$ and $V_\gamma$ are the volumes of ferrite and austenite phases respectively. Noting that there is no source or sink of any substance and that the flow of material at the boundary of a phase is due to both local vacancy-atom exchange and the migration of boundaries, Eq. (4) can be recast using Stokes theorem as:

$$\int_{S_\delta} \mathbf{n}_\delta \cdot \left(\mathbf{J}_i^\delta + C_i^\delta \mathbf{u}\right) dS + \int_{S_\gamma} \mathbf{n}_\gamma \cdot \left(\mathbf{J}_i^\gamma + C_i^\gamma \mathbf{u}\right) dS = 0, \tag{5}$$

where $S$ indicates boundary of a phase, $\boldsymbol{J_i}$ is the concentration flow of material at the boundary, $\mathbf{u}$ is the velocity of boundary migration and $\mathbf{n}$ is the outwards normal vector of the boundary. Suppose that the interphase boundary is the only region where material flow occurs and noting that $\mathbf{n}_\delta = -\mathbf{n}_\gamma$, Eq. (5) is then simplified as:

$$\int_A \left(J_i^\delta + J_i^\gamma\right) + \left(C_i^{\delta e} - C_i^{\gamma e}\right) u\, dA = 0, \tag{6}$$

where A is the area of the interface, $J_i^\delta = \mathbf{n}_\delta \cdot \mathbf{J}_i$, $J_i^\gamma = \mathbf{n}_\gamma \cdot \mathbf{J}_i$ and $u = \mathbf{n}_\delta \cdot \mathbf{u}$. Since the interface is a vacancy reservoir, we suppose that the concentration of either austenite or ferrite forming elements near the interface can quickly approach the equilibrium magnitude. Therefore, the concentrations at the both sides of interface A in Eq. (6) has been replaced by the equivalent values $C_i^{\delta e}$ and $C_i^{\gamma e}$. Apparently, the migration velocity $u$ of the phase boundary cannot depend on the species in diffusion i. Therefore, the total flow into the phase boundary from both sides $J_i = \left(J_i^{\delta} + J_i^{\gamma}\right)$ must satisfy the constraint of Eq. (6) for any substance $i$. The subscript $i$ is removed in the following discussion since solution from any substance shall be identical. If the total flow into the interphase boundary $J$ is time-independent, the velocity $u$ becomes constant. The kinetics of phase growth then mainly depends on the geometry of the phase. For example, for a uniform nucleation and spherical growth, Avrami's theory renders: $\phi_{\gamma} \sim 1 - \exp\left(-kt^4\right)$, where $\phi_{\gamma}$ is the volume fraction of austenite phase which grows from the ferrite phase in the isothermal hold. The general Avrami scaling is given as: $\phi_{\gamma} \sim 1 - \exp\left(-kt^n\right)$, where the fact that $n < 4$ is generally attributed to non-spherical growth. For current material, the flow $J$ can hardly be treated to be time-impendent since it depends on the deviation from the equilibrium concentration, which must diminish when time increase. Therefore, the concentration near the boundary is alternatively assumed a Gauss error function:

$$C^{\delta(\gamma)}(x,t) = C^{\delta e(\gamma e)} + \left(C_0^{\delta(\gamma)} - C^{\delta e(\gamma e)}\right)\left(1\text{-}\operatorname{erf}\left(\frac{x}{2\sqrt{D_{\delta(\gamma)}t}}\right)\right), \tag{7}$$

which arises from the transient solution of the Fick's second law for a one-dimensional diffusion. The subscript "0" indicates the value at $t = 0$, the variable $x$ is the distance from the interface and $D$ is the diffusion constant. Using the Fick's first law, the time-dependence of $J_i$ can be given in the form as:

$$J = -\left(D_{\delta}\frac{\partial C^{\delta}}{\partial x} + D_{\gamma}\frac{\partial C^{\gamma}}{\partial x}\right) = \left(\frac{C_0^{\delta} - C^{\delta e}}{\sqrt{\pi D_{\delta}}} + \frac{C_0^{\gamma} - C^{\gamma e}}{\sqrt{\pi D_{\gamma}}}\right)\frac{1}{\sqrt{t}}, \tag{8}$$

which indicates that the migration of the interphase boundary satisfies the scaling

$$u \sim \frac{1}{\sqrt{t}}\,. \tag{9}$$

Now considering a spherical growth from an austenite nucleus, the volume of this austenite phase $V_1$ at time $t$ should follow the scaling:

$$V_1 \sim t^{3/2}, \tag{10}$$

since $\frac{d\left(V_1^{1/3}\right)}{dt} \sim u \sim \frac{1}{\sqrt{t}}$ due to Eq. (9).

Considering a constant nucleating rate from the remaining ferrite phase and noting that only the fraction $\left(\phi^e - \phi\right)$ is the net nucleation for austenite phase, the Avrami's argument on uniform nucleation leads to:

$$d\phi_\gamma \sim \left(\phi_\gamma^e - \phi_\gamma\right)\left(t-\tau\right)^{3/2} d\tau\,, \tag{11}$$

which leads to

$$f = \phi_\gamma / \phi_\gamma^e = 1 - \exp\left(-\left(t/\tau\right)^{5/2}\right), \tag{12}$$

where $n = 2.5$ is obtained and used in apprehending experimental results.

### 4.2 The role of plastic deformation in phase transformation

It is well known that rolling leads to “pancake” grains, which is an effective approach to obtain small grains in the process involving phase transformation, since nucleation of new phase preferably starts at grain boundaries and the pancake-shaped grains limited the space of grain growth.

It is also conceived that severe plastic deformation induces more internal energy owing to the high density of defects, which shall bring about faster phase transformation. However, this is not true in our case. In Table 2, the time $\tau$ indicates the characteristic time for phase transformation. Comparing $\tau$ of AC and CR samples at different temperatures, it is noted that the ferrite-to-austenite phase transformation of CR sample is slower than that of AC. And the plastic deformation reduces not only the rate of phase transformation but also the equilibrium content of $\gamma$ phase.

To corroborate the effect of plastic deformation, the AC and CR samples were investigated using differential scanning calorimeter (DSC, PerkinElmer DSC7) under the heating rate of 25 °C/min, as show in Fig. 8. For the AC and CR samples, the exothermic peaks at about 570 and 620 °C are found respectively, which indicates that the plastic deformation defers the ferrite-to-austenite transformation. The metallographs at the temperatures before and after the peak are shown in the inset. Fig. (a) and Fig. (b) pertain to the samples AC-550-30-W and AC-600-30-W, and the newly-nucleated $\gamma_2$ phase can be found in (b) but no $\gamma_2$ in (a). Similarly, the metallographs of the sample CR-600-30-W (inset (c)) has no $\gamma_2$, while that of CR-650-30-W (inset (d)) has.

The DSC results confirm that plastic deformation supresses the ferrite-to-austenite transformation at low temperature. In DSS, $\delta$ ferrite is the metastable phase [1, 7, 24] at room temperature, which remains owing to the fast cooling. Therefore, the $\delta$-to-$\gamma$ transformation at an elevated temperature is a transition from the metastable to the stable phase and must be exothermic as indicated by the

DSC peaks shown in Fig. 8. When temperature is sufficiently high, the γ-to-δ transition occurs, which becomes endothermic. Noting that plastic deformation introduces additional mechanical energy to the material owing to the distorted lattices surrounding defects, this additional energy supresses the exothermic reaction, as manifested by the retarded ferrite-to-austenite transformation at low temperature, but help the endothermic one, as manifested by the fact that the CR samples achieve the fully ferritic structure at the lower temperature than that of AC counterparts (Fig. 3(II)). Higher temperature makes the atomic system more active and reduces microstructure defects. Therefore the effect of plastic deformation should be reduced with the increase of temperature. On the other hand, higher temperature leads to less equilibrium content of γ phase. The combination of these two effects, as sketched in Fig. 9, makes the equilibrium content of γ phase in CR samples approaches a maximum magnitude at about 850 °C, which explains the difference between Fig. 6(a) and Fig. 6(b). And the shaded area in Fig. 9 quantifies the effect of plastic deformation at different temperatures.

## 5. Conclusion

This work investigates the effect of annealing temperature and time, cooling rate, and plastic deformation on the phase transformation of 15Cr-2Al-2Ni-11Mn. The main findings are:

1. The primary phase transformation is ferrite-to-austenite when the annealing temperature is less than 1050 °C, but becomes austenite-to-ferrite at higher

temperature for rapidly-solidified DSS 15Cr-2Al-2Ni-11Mn.

2. It is found that plastic deformation not only changes the rate of phase transformation and the grain size of new phase but also changes the equilibrium phase constitution. Plastic deformation suppress the transformation from ferrite to austenite phase, while promotes the inverse one. After 70% cold rolling, the maximum austenitic content after long isothermal annealing occurs at about 850 °C. This effect of plastic deformation has never been reported before.

3. Based on Avrami equation, TTT diagrams of as-cast and cold-rolled samples were established. It is found that the stretched exponent $n$ is about 2.5 by fitting the experimental data, which can be explained based on a simplified model of diffusion-mediated phase transformation.

## Acknowledgement

This work was supported by the Early Career Scheme (ECS) of the Hong Kong Research Grants Council (Grant No. 25200515) and the Departmental General Research Funds (G-UA2L) of Hong Kong Polytechnic University. We are grateful for the support.

## Reference

[1] J.-O. Nilsson. Super duplex stainless steels, Materials Science and Technology 8 (1992) 685-700.

[2] S.-G. Wang, G.-P. Dong, Q.-H. Ma. Welding of duplex stainless steel composite plate: influence on microstructural development, Materials and Manufacturing Processes 24 (2009) 1383-1388.

[3] Y.-C. Hsieh, L. Zhang, T.-F. Chung, Y.-T. Tsai, J.-R. Yang, T. Ohmura, T. Suzuki. In-situ transmission electron microscopy investigation of the deformation behavior of spinodal nanostructured δ-ferrite in a duplex stainless steel, Scripta Materialia 125 (2016) 44-48.

[4] Z. Zhang, H. Jing, L. Xu, Y. Han, L. Zhao. Investigation on microstructure evolution and properties of duplex stainless steel joint multi-pass welded by using different methods, Materials & Design 109 (2016) 670-685.

[5] D. Xu, J. Xia, E. Zhou, D. Zhang, H. Li, C. Yang, Q. Li, H. Lin, X. Li, K. Yang. Accelerated corrosion of 2205 duplex stainless steel caused by marine aerobic Pseudomonas aeruginosa biofilm, Bioelectrochemistry 113 (2017) 1-8.

[6] S.R. Chen, H.A. Davies, W.M. Rainforth. Austenite phase formation in rapidly solidified Fe–Cr–Mn–C steels, Acta Materialia 47 (1999) 4555-4569.

[7] J. Wan, Q. Ran, J. Li, Y. Xu, X. Xiao, H. Yu, L. Jiang. A new resource-saving, low chromium and low nickel duplex stainless steel 15Cr–xAl–2Ni–yMn, Materials & Design 53 (2014) 43-50.

[8] A.L. Schaeffler. Selection of austenitic electrodes for welding dissimilar metals, Welding journal 26 (1947) 601-620.

[9] S. Sohn, B.-J. Lee, S. Lee, N. Kim, J.-H. Kwak. Effect of annealing temperature on microstructural modification and tensile properties in 0.35 C–3.5 Mn–5.8 Al lightweight steel, Acta Materialia 61 (2013) 5050-5066.

[10] S. Li, Y. Wang, X. Wang. Effects of ferrite content on the mechanical properties of thermal aged duplex stainless steels, Materials Science and Engineering: A 625 (2015) 186-193.

[11] L. Chen, H. Tan, Z. Wang, J. Li, Y. Jiang. Influence of cooling rate on microstructure evolution and pitting corrosion resistance in the simulated heat-affected zone of 2304 duplex stainless steels, Corrosion Science 58 (2012) 168-174.

[12] H.-S. Cho, K. Lee. Effect of cold working and isothermal aging on the precipitation of sigma phase in 2205 duplex stainless steel, Materials Characterization 75 (2013) 29-34.

[13] S. Tavares, M. Da Silva, J. Pardal, H. Abreu, A. Gomes. Microstructural changes produced by plastic deformation in the UNS S31803 duplex stainless steel, Journal of Materials Processing Technology 180 (2006) 318-322.

[14] Y.-J. Kim, L.S. Chumbley, B. Gleeson. Determination of isothermal transformation diagrams for sigma-phase formation in cast duplex stainless steels CD3MN and CD3MWCuN, Metallurgical and Materials Transactions A 35 (2004) 3377-3386.

[15] E. Johnson, Y.-J. Kim, L.S. Chumbley, B. Gleeson. Initial phase transformation diagram determination for the CD3MN cast duplex stainless steel, Scripta materialia 50 (2004) 1351-1354.

[16] H. Sieurin, R. Sandström. Austenite reformation in the heat-affected zone of duplex stainless steel 2205, Materials Science and Engineering: A 418 (2006) 250-256.

[17] H. Hemmer, Ø. Grong. A process model for the heat-affected zone microstructure evolution in duplex stainless steel weldments: Part I. the model, Metallurgical and Materials Transactions A 30 (1999) 2915-2929.

[18] A. Ramirez, J. Lippold, S. Brandi. The relationship between chromium nitride and secondary austenite precipitation in duplex stainless steels, Metallurgical and materials transactions A 34 (2003) 1575-1597.

[19] T. Chen, J. Yang. Effects of solution treatment and continuous cooling on σ-phase precipitation in a 2205 duplex stainless steel, Materials Science and Engineering: A 311 (2001) 28-41.

[20] J.W. Christian. The Theory of Transformations in Metals and Alloys Ediz 2. an Advanced Textbook in Physical Metallurgy Parte 1. Equilibrium and General Kinetic Theory, Pergamon Press, 1975.

[21] R. Magnabosco. Kinetics of sigma phase formation in a duplex stainless steel, Materials Research 12 (2009) 321-327.

[22] H. Hemmer, Ø. Grong, S. Klokkehaug. A process model for the heat-affected zone microstructure evolution in duplex stainless steel weldments: Part II. Application to electron beam welding, Metallurgical and Materials Transactions A 31 (2000) 1035-1048.

[23] W. Zhang, T. DebRoy, T. Palmer, J. Elmer. Modeling of ferrite formation in a duplex stainless steel weld considering non-uniform starting microstructure, Acta Materialia 53 (2005) 4441-4453.

[24] R. Badji, M. Bouabdallah, B. Bacroix, C. Kahloun, B. Belkessa, H. Maza. Phase transformation and mechanical behavior in annealed 2205 duplex stainless steel welds, Materials Characterization 59 (2008) 447-453.

## List of Captions

Table 1 The specific chemical compositions of the 15Cr-2Ni DSS (wt.%)

Table 2 Fitting parameters of Avrami equation for ferrite-to-austenite transformation in DSS

Table 3 Mechanical property of DSS samples

Fig. 1 An overview of metallographs (a, c~f) and XRD pattern (b) of DSS samples: (a) CR-1050-30-W, (b) CR-1050-30-W, CR-1050-30-A and CR-1050-30-F, (c) CR-850-30-W, (d) CR-850-90-W, (e) CR-850-30-F and (f) AC-850-30-W

Fig. 2 The typical TEM images taken from $\delta/\gamma$ interface of CR sample solution-treated at 750 °C for 30 min followed by water quenching

Fig. 3 The variation of room-temperature ferrite content with annealing temperature: the samples were held for (I) 30 min and (II) a sufficiently long time followed by water quenching, respectively. The inset shows the effect of air cooling and furnace cooling for (I).

Fig.4 The metallographs of samples (a) CR-950-1-W and (b) CR-1150-0.17-W for demonstrating nucleation of $\gamma_2$ phase

Fig. 5 Experimental results and fitting curves on the temperature-time dependent variation of austenite content plotted in log-log-scale

Fig. 6 TTT diagram of austenitic volume fraction of (a) as-cast and (b) cold-rolled samples

Fig. 7 Metallographs of samples CR-1000-15-A, CR-750-90-A, CR-1000-30-A, AC-1000-30-A and AC-750-180-W before tensile test

Fig. 8 DSC curves of as-cast and cold-rolled samples. The insets show the metallographs before and after the exothermic peak.

Fig. 9 The effect of plastic deformation on austenite formation of DSS samples

**Table**

Table 1 The specific chemical compositions of 15Cr-2Ni DSS (wt.%).

| Element | Fe | Cr | Al | Ni | Mn | C |
|---|---|---|---|---|---|---|
| Wt.% | Balance | 15.27 | 1.96 | 2.04 | 11.05 | 0.02 |

## Table

Table 2 Fitting parameters of Avrami equation for ferrite-to-austenite transformation in DSS

| | $T$ (℃) | $\tau$ (min) | $n$ | $t_0$ (min) | $\phi_{\gamma}^{e}$ (%) |
|---|---|---|---|---|---|
| As-cast | 750 | 305.40 | 2.80 | 280.00 | 54 |
| | 850 | 192.90 | 2.30 | 200.00 | 48 |
| | 950 | 61.10 | 2.49 | 60.00 | 46 |
| | 1050 | 11.30 | 2.80 | 12.00 | 43 |
| Cold-rolled | 750 | 364.30 | 2.60 | 399.00 | 41 |
| | 850 | 246.50 | 2.50 | 253.00 | 46 |
| | 950 | 62.90 | 2.52 | 68.50 | 44 |
| | 1050 | 12.00 | 2.69 | 13.20 | 41 |

**Table**

Table 3 Mechanical property of DSS samples

| Samples | Yield strength (MPa) | Ultimate tensile Strength (MPa) | Elongation (%) | Austenite content (%) |
|---|---|---|---|---|
| CR-1000-15-A | 499 | 718 | 21 | 48 |
| CR-750-90-A | 371 | 631 | 37 | 51 |
| CR-1000-30-A | 349 | 596 | 28 | 50 |
| AC-1000-30-A | 306 | 548 | 32 | 54 |
| AC-750-180-W | 300 | 564 | 27 | 53 |

**Figure**

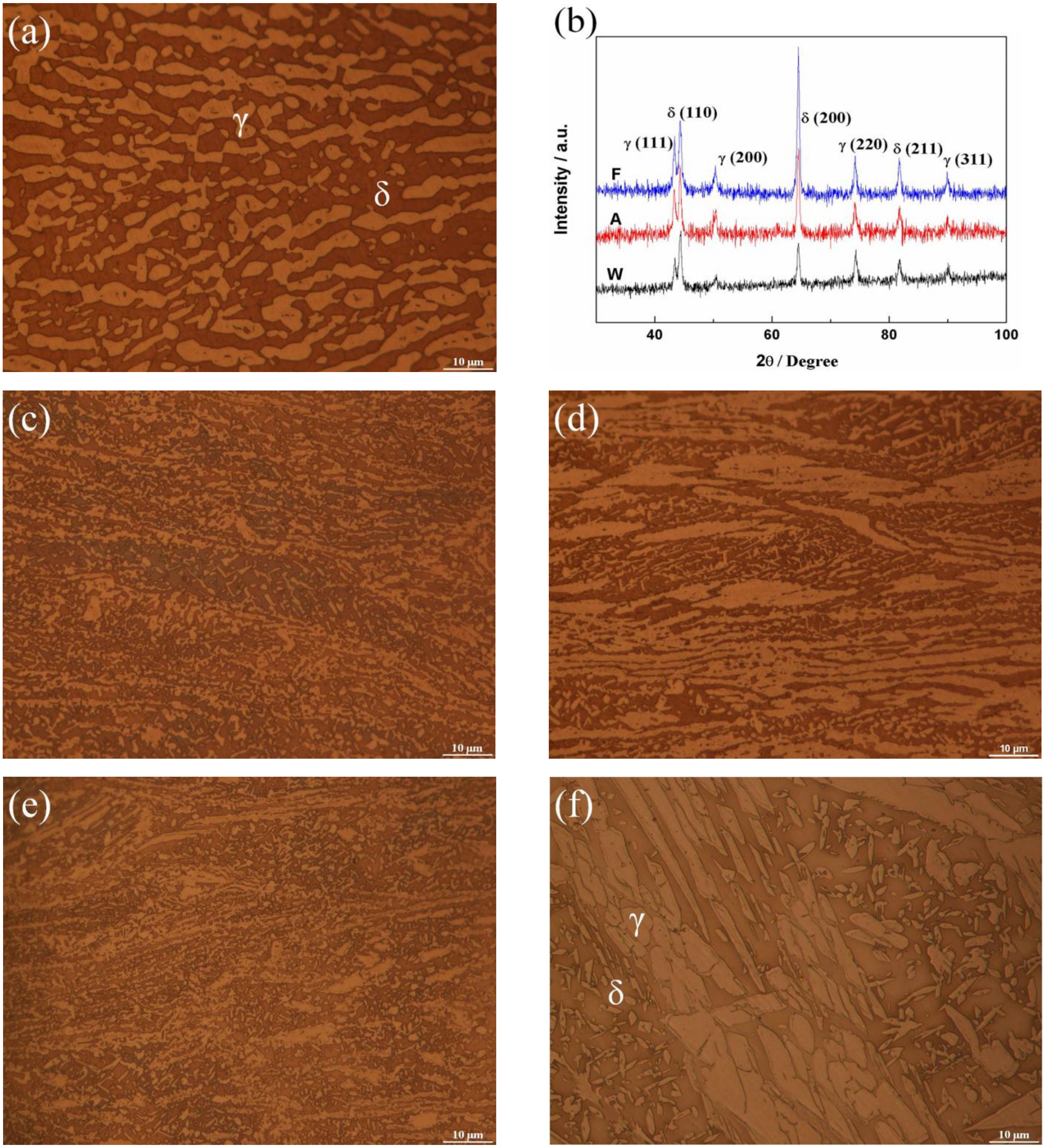

Fig. 1 An overview of metallographs (a, c~f) and XRD pattern (b) of DSS samples: (a) CR-1050-30-W, (b) CR-1050-30-W, CR-1050-30-A and CR-1050-30-F, (c) CR-850-30-W, (d) CR-850-90-W, (e) CR-850-30-F and (f) AC-850-30-W

**Figure**

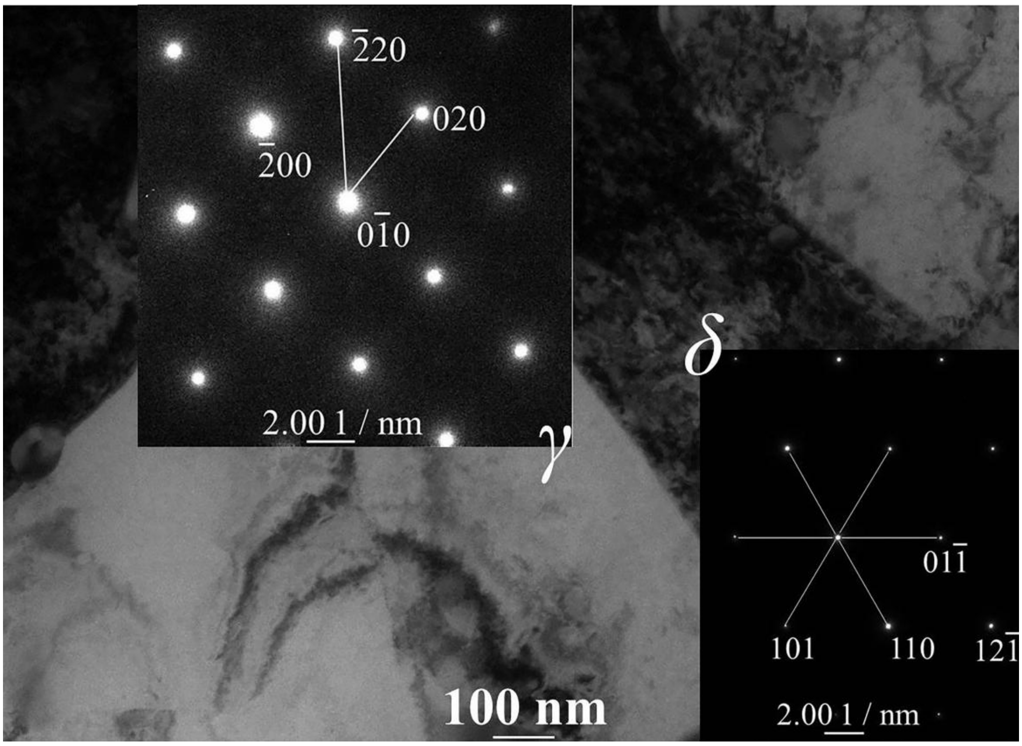

Fig. 2 The typical TEM images taken from δ/γ interface of CR sample solution-treated at 750 °C for 30 min followed by water quenching

**Figure**

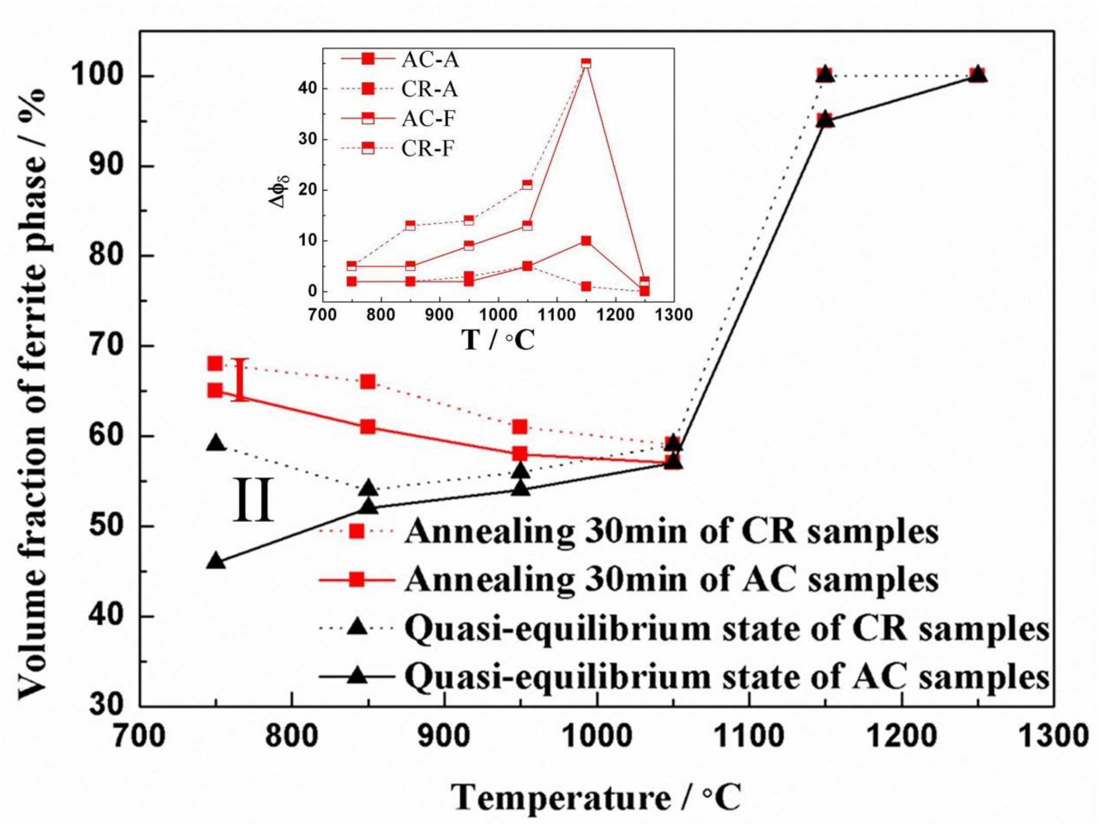

Fig. 3 The variation of room-temperature ferrite content with annealing temperature: the samples were held for (I) 30 min and (II) a sufficiently long time followed by water quenching, respectively. The inset shows the effect of air cooling and furnace cooling for (I).

**Figure**

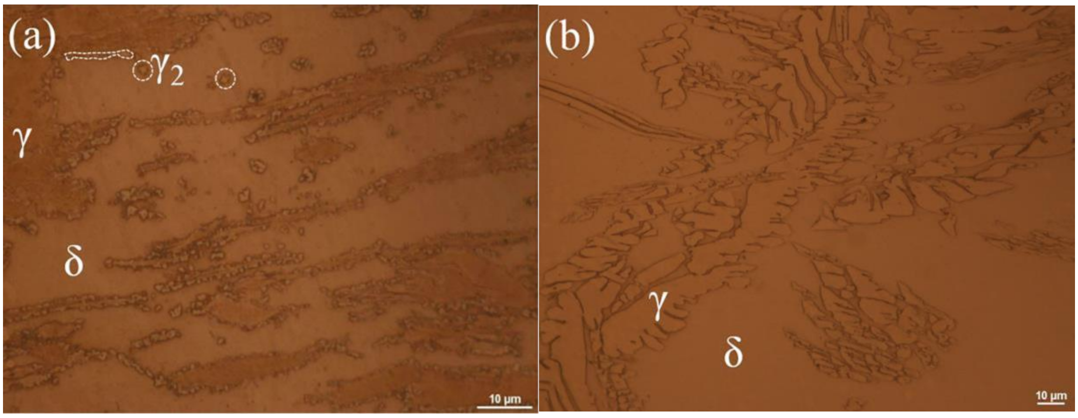

Fig.4 The metallographs of samples (a) CR-950-1-W and (b) CR-1150-0.17-W for demonstrating nucleation of $\gamma_2$ phase

Figure

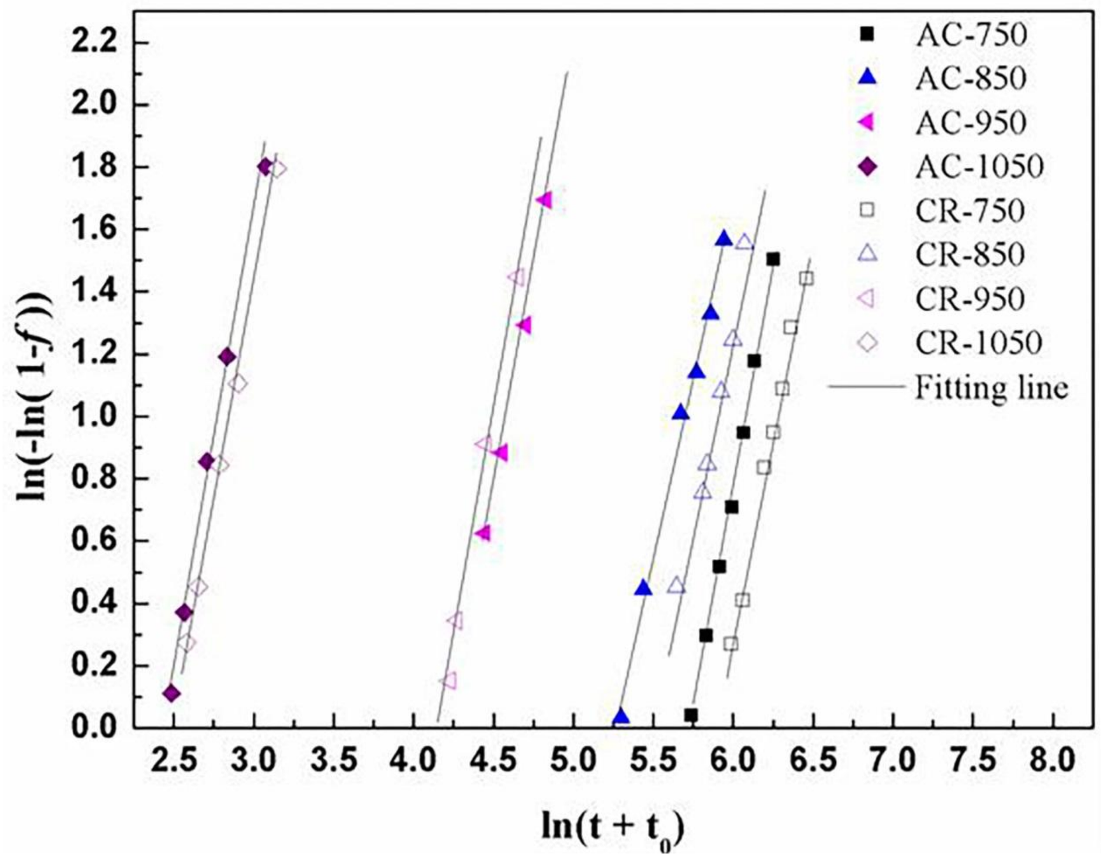

Fig. 5 Experimental results and fitting curves on the temperature-time dependent variation of austenite content plotted in log-log-scale

**Figure**

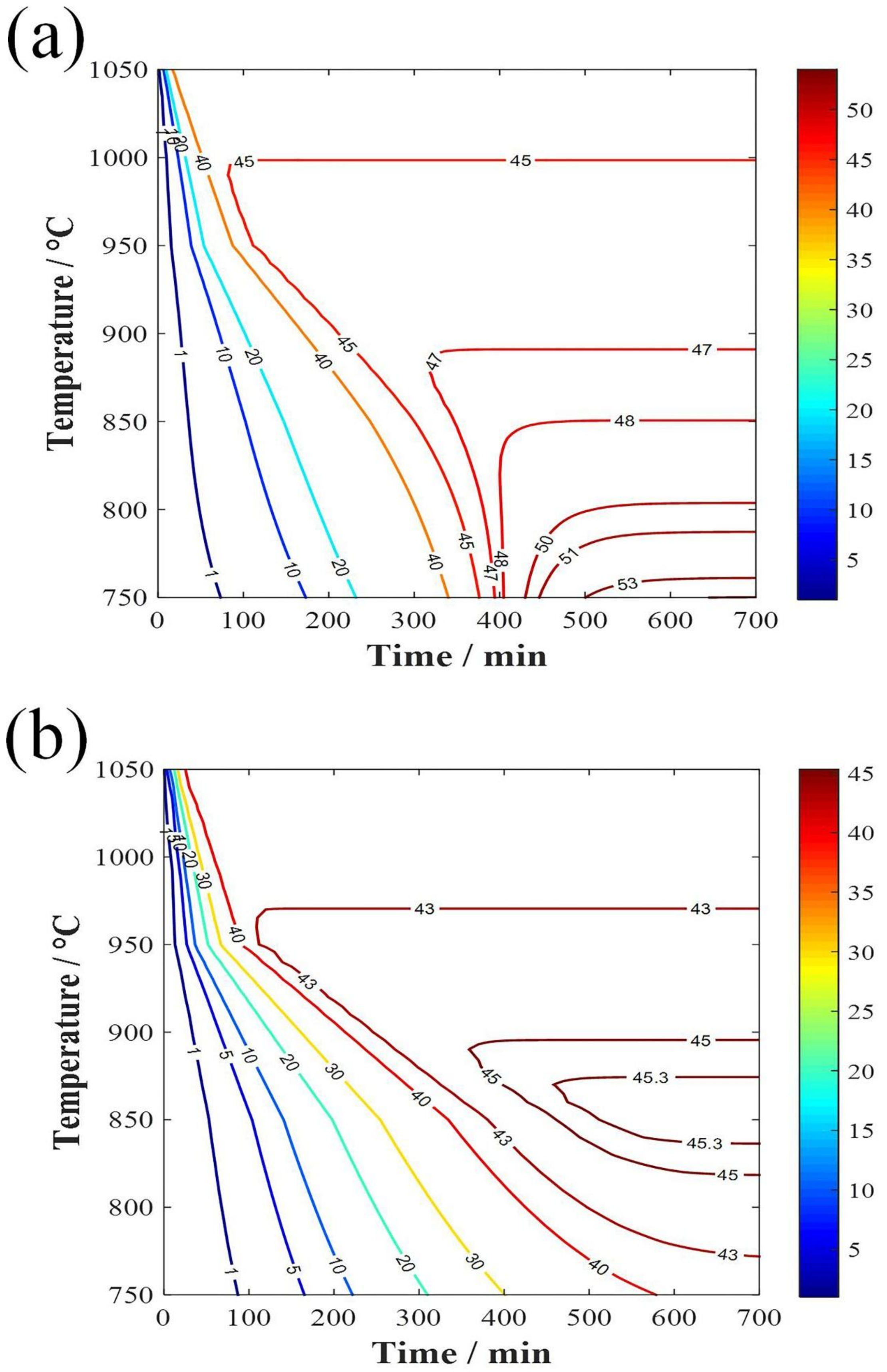

Fig. 6 TTT diagram of austenitic volume fraction of (a) as-cast and (b) cold-rolled samples

**Figure**

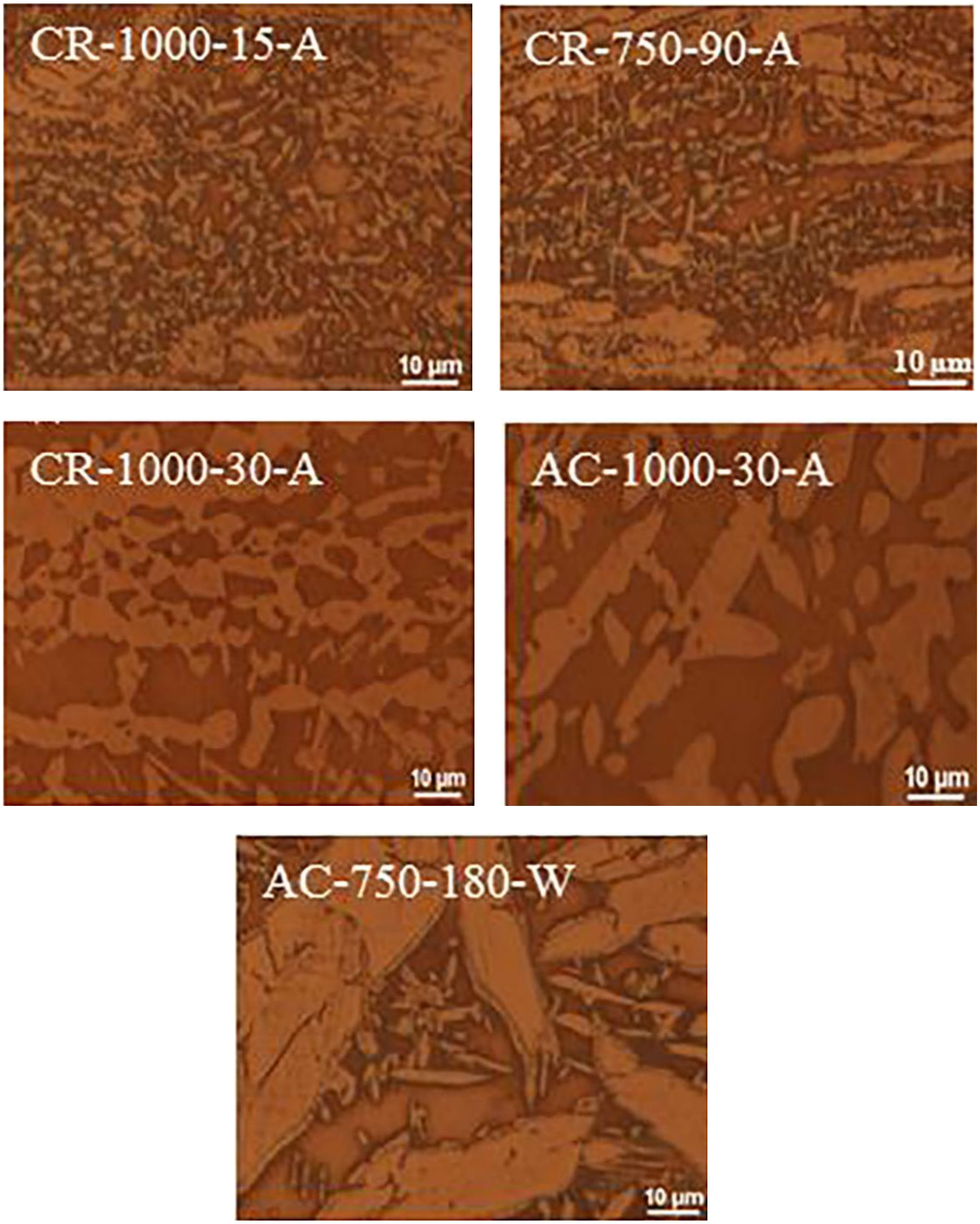

Fig.7 Metallographs of samples CR-1000-15-A, CR-750-90-A, CR-1000-30-A, AC-1000-30-A and AC-750-180-W before tensile test

Figure

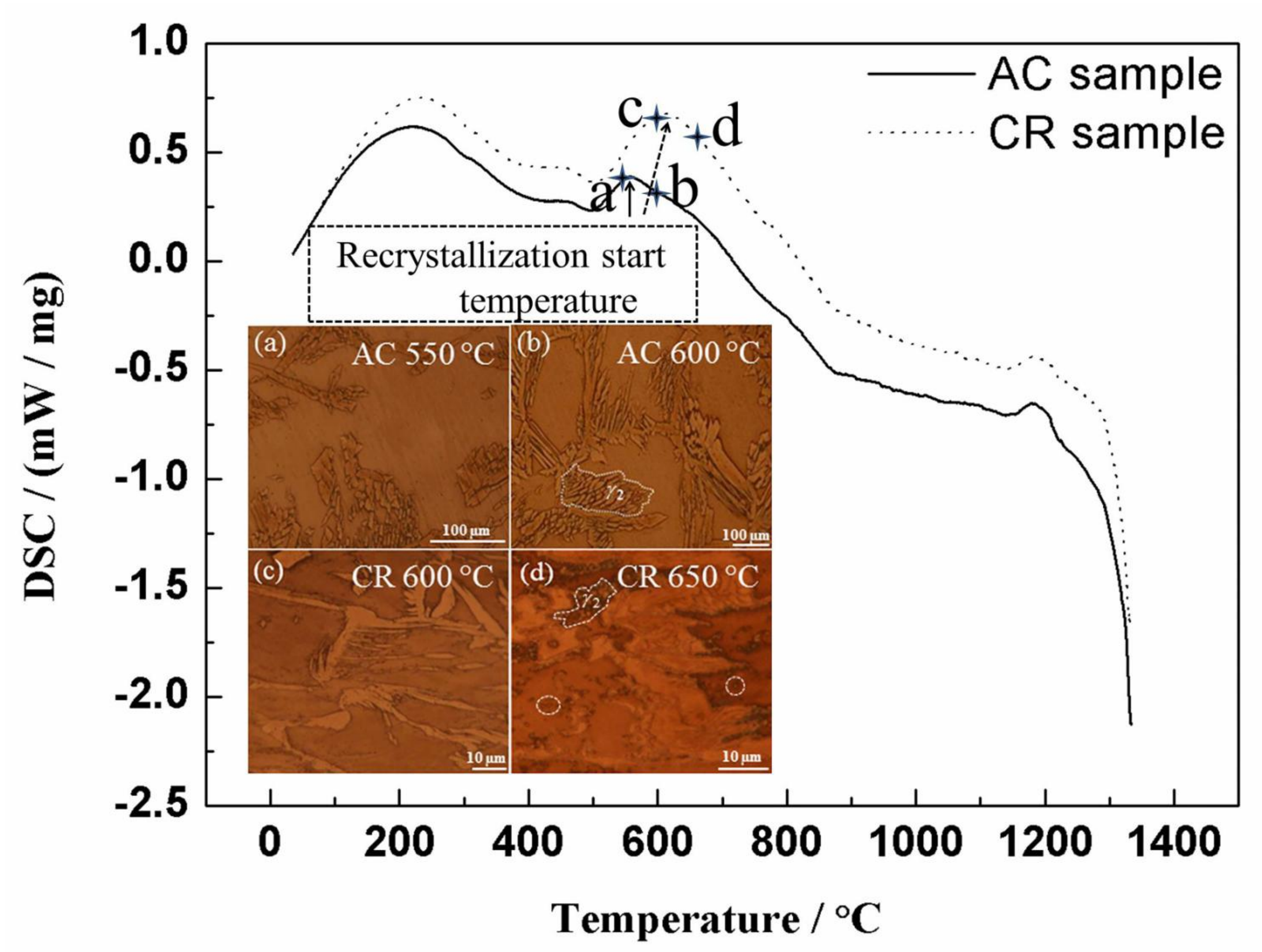

Fig. 8 DSC curves of as-cast and cold-rolled samples. The insets show the metallographs before and after the exothermic peak.

**Figure**

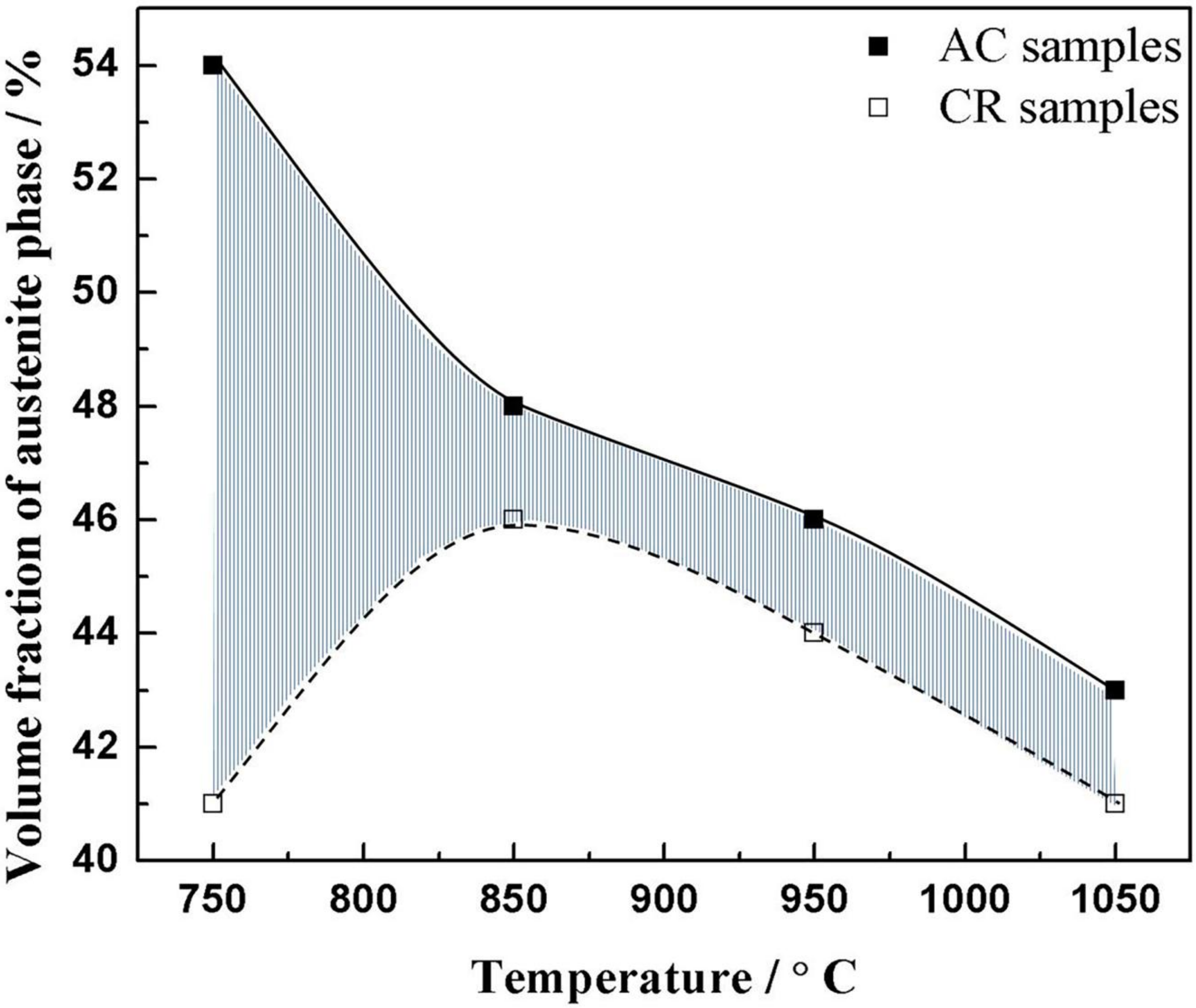

Fig.9 The effect of plastic deformation on austenite formation of DSS samples